

The extended Main Sequence Turnoff of the Milky Way open cluster Collinder 347

Andrés E. Piatti^{1,2*} and Charles Bonatto³

¹ Consejo Nacional de Investigaciones Científicas y Técnicas, Godoy Cruz 2290, C1425FQB, Buenos Aires, Argentina

² Observatorio Astronómico de Córdoba, Laprida 854, 5000, Córdoba, Argentina

³ Departamento de Astronomia, Universidade Federal do Rio Grande do Sul, Av. Bento Gonçalves 9500 Porto Alegre 91501-970, RS, Brazil

Accepted XXX. Received YYY; in original form ZZZ

ABSTRACT

We made use of the *Gaia* DR2 archive to comprehensively study the Milky Way open cluster Collinder 347, known until now as a very young object of solar metal-content. However, the G versus $G_{BP} - G_{RP}$ colour-magnitude diagram (CMD) of *bonafide* probable cluster members, selected on the basis of individual stellar proper motions, their spatial distribution and placement in the CMD, reveals the existence of a Hyades-like age open cluster ($\log(t/\text{yr}) = 8.8$) of moderately metal-poor chemical content ($[\text{Fe}/\text{H}] = -0.4$ dex), with a present-day mass of $3.3 \times 10^3 M_{\odot}$. The cluster exhibits an extended Main Sequence turnoff (eMSTO) of nearly 500 Myr, while that computed assuming Gaussian distributions from photometric errors, stellar binarity, rotation and metallicity spread yields an eMSTO of ~ 340 Myr. Such an age difference points to the existence within the cluster of stellar populations with different ages.

Key words: (Galaxy:) open clusters and associations: general – (Galaxy:) open clusters and associations: individual – technique: photometric.

1 INTRODUCTION

Extended Main-Sequence Turnoffs (eMSTOs) have recently been confirmed to be a common feature in the colour-magnitude diagrams (CMDs) of Milky Way open clusters (Cordoni et al. 2018). It has gained an increasing consensus that its origin could be linked to stellar rotation (Bastian et al. 2018; Sun et al. 2019; Li et al. 2019). Indeed, Marino et al. (2018b,a) spectroscopically measured different rotational velocities of Main Sequence stars of Milky Way open clusters and Magellanic Cloud clusters with observed eMSTOs. However, other previous works have concluded that age variation, together with rotation, are necessary to explain the eMSTO (Gossage et al. 2019, and references therein). D’Antona et al. (2017) have suggested that if the bluest stars in the eMSTO are interpreted as stars initially rapidly rotating, but that have later slowed down, the age difference disappears, and “braking” also helps to explain the apparent age differences of the eMSTO (see also Georgy et al. 2019).

Besides eMSTOs, clusters younger than ~ 1 Gyr also exhibit split Main Sequences (see Milone et al. 2018, and references therein). The comparison between the observations and isochrones suggests that the blue Main Sequences are

made of slow-rotating stars, while the red ones host stars with rotational velocities close to the breakup value. Note that there would be a minimum mass for rotating stars in order to make MSTOs significantly wider than the rest of the cluster’s Main Sequence (Goudfrooij et al. 2018). Large populations of Be stars, which are fast-rotating stars, have also been detected (Bastian et al. 2017; Dupree et al. 2017).

Here we report a serendipitous discovery for an open cluster, Collinder 347, to exhibit an eMSTO much wider than that predicted considering altogether photometric uncertainties, binarity, metallicity spread and stellar rotation. The finding is twofold, because the cluster was known to be young (< 15 Myr) and of solar metal content (Bukowiecki et al. 2011; Kharchenko et al. 2013; Clariá et al. 2019), but we show that it would seem to be a Hyades-like age cluster with a moderately metal-poor overall abundance. The anomalous wide eMSTO of Collinder 347 deserves further investigation to answer the very question about whether it could come from an intrinsic age spread. If such a hypothesis were confirmed, it would impact in the way we understand how star clusters could form and evolve.

In Section 2 we describe the used data sets and the applied filtering criteria in order to select probable cluster members. Section 3 deals with the cluster structural and astrophysical properties estimates, while in Section 4 we discuss the unveiled cluster eMSTO.

* E-mail: andres.piatti@unc.edu.ar

2 DATA HANDLING

We used the *Gaia* DR2 archive¹ to retrieve astrometric positions (RA,DEC, l,b), proper motions in Right Ascension (pmra) and Declination (pmdec) and G, G_{BP}, G_{RP} photometry of stars in a field of $2^\circ \times 2^\circ$ centred on Collinder 347. We limited our sample to stars with excess noise ($\text{sepsi} < 2$) and significance of excess of noise ($\text{sepsi} < 1$) to prune the data (Lindegren et al. 2018; Piatti et al. 2019). Top-left panel of Fig. 1 shows a group of stars inside the drawn circle that arises as an overdensity in the vector proper motion diagram; they clearly reveal Collinder 347 on the sky (see the top-right panel). Furthermore, the group of stars encircled within the central circle mainly define the cluster CMD (bottom-right panel), which seems to correspond to a populous and intermediate-age open cluster. The radius of that circle is the cluster radius ($\log(r_{cls} / \text{arcsec}) = 3.0$), defined as the intersection of the cluster stellar radial profile with the mean background level (see bottom-left panel of Fig. 1).

We first inspected to quality of the kinematic and photometric information of all the stars located inside both, the circle in the vector proper motion diagram and the central circle in the finding chart. Fig. 2 shows that there is no dependence of the individual proper motions with the G magnitude nor with the distance r from the cluster centre. Their uncertainties increase with the G magnitude, as expected. As for the *Gaia* DR2 photometry, there would seem to be no trend with crowding. Furthermore, according to Arenou et al. (2018, see Section 3), the *Gaia* DR2 photometry completeness is $\gtrsim 90$ per cent for stars with $G < 19$ mag in the inner region of a globular cluster with $\sim 10^4$ stars/sq deg, so that we deal with basically a complete photometry data sets.

In order to clean the cluster CMD from the contamination of field stars with similar cluster kinematics projected along the cluster line-of-sight, we used as reference six circular regions distributed around the cluster circle as shown in Fig. 1 (top-right panel). For each reference star field CMD, we generated a sample of boxes ($G_o, (G_{BP} - G_{RP})_o$) centred on each star, with sizes ($\Delta(G), \Delta(G_{BP} - G_{RP})$) defined in such a way that one of their corners coincides with the closest star in that CMD region. The intrinsic G_o magnitudes and $(G_{BP} - G_{RP})_o$ colours were computed from individual $E(B - V)$ reddenings obtained from the interstellar absorption maps produced by Lallement et al. (2019), and the relationships $A_G = 2.44 E(B - V)$ and $E(G_{BP} - G_{RP}) = 1.27 E(B - V)$ (Cardelli et al. 1989; Wang & Chen 2019). Lallement et al. (2019) used the *Gaia* DR2 and 2MASS photometric data sets to estimate the extinction towards ~ 27 millions carefully selected stars, from which a 3D map of Milky Way interstellar dust within 3 kpc from the Sun was generated. The mean differential-reddening resolution is 0.003 mag/pc.

Details of the procedure of representing the reference star field CMD with an assembly of boxes can be found in Piatti & Bica (2012) and Piatti et al. (2018). It has the advantage of accurately reproducing the reference star field in terms of stellar density, luminosity function and colour distribution. Note that this also implies to consider the variations of the interstellar reddening across the cluster field.

The generated box sample of each reference star field CMD was superimposed at a time to the cluster CMD and subtracted from it one star per box; that closest to the box centre. We merged all the six cleaned cluster CMDs and produced one with membership probabilities (P) on the basis of the number of times a star kept unsubtracted. In the subsequent analysis we only retain star with $P > 90$ per cent, i.e., the most probable cluster members as judged by their kinematics, spatial distribution in the cluster field and position in the cluster CMD.

Fig. 3 illustrates the spatial distributions (left panel) and the intrinsic cluster CMD (right panel) of stars with $P > 90$ per cent, respectively. We have coloured the stars according to the reddening values provided by Lallement et al. (2019), which were used to obtain the intrinsic magnitudes and colours. As can be seen, the total differential reddening across the cluster field amounts ~ 0.14 mag, which represents a spatial reddening variation of ~ 0.003 mag/pc ($= 0.006$ mag/arcmin). The errors of the individual $E(B - V)$ values spans the range 0.095 - 0.115 mag, which could blur any signature in the cluster CMD with a resolution smaller than ~ 0.10 mag. Nevertheless, it does not appear to be any differential reddening effects affecting the distribution of stars along the cluster's Main Sequence. For instance, reddest Main Sequence stars – particularly those grouped around $G_o \approx 12.0$ mag and $(G_{BP} - G_{RP})_o \sim 0.25$ mag – are spread over the whole cluster field, i.e., they come from cluster regions with different $E(B - V)$ values.

3 CLUSTER'S ASTROPHYSICAL PROPERTIES

Fig. 4 (panel a) shows the resulting intrinsic cluster CMD for stars with $P > 90$ per cent. At first glance, there is no evidence for Collinder 347 to be a young open cluster, but one of intermediate-age. In order to estimate its age, distance and metallicity, we used that CMD to which we superimposed a subset of theoretical isochrones computed by Bressan et al. (2012). Taking into account as a reference the colour difference between the red clump and the MSTO, and the curvature and its extent of the lower envelope of the upper Main Sequence, we restricted the isochrone sample to those with $8.5 < \log(t / \text{yr}) < 9.1$, in steps of $\Delta(\log(t / \text{yr})) = 0.05$, and metallicities spanning almost all the Galactic open cluster metallicity range, namely, $-0.8 < [\text{Fe}/\text{H}] (\text{dex}) < +0.2$ (Heiter et al. 2014), in steps of $\Delta[\text{Fe}/\text{H}] = 0.10$ dex. We fitted all possible isochrone combination and found that it is necessary to allow isochrones spanning a range of ages in order to satisfactorily reproduce the upper Main Sequence bluest and reddest envelopes, simultaneously, provided that all of them are fitted using the the same true distance modulus and metallicity. Particularly, we found that $\langle (m - M)_o \rangle = (10.70 \pm 0.15)$ mag, equivalent to a Galactocentric distance of $R_{GC} = 6.9$ kpc, $\langle [\text{Fe}/\text{H}] \rangle = (-0.40 \pm 0.15)$ dex and $\log(t / \text{yr}) = 8.80 - 9.05$, provide with the best resemblance of the cluster CMD. The youngest isochrone reproduces at a $\sigma(\log(t / \text{yr})) = 0.05$ level the bluest lower and upper parts of the cluster Main Sequence, simultaneously, while that of $\log(t / \text{yr}) = 8.9$ could be associated to the mean fiducial cluster Main Sequence. The cluster CMD

¹ <http://gea.esac.esa.int/archive/>

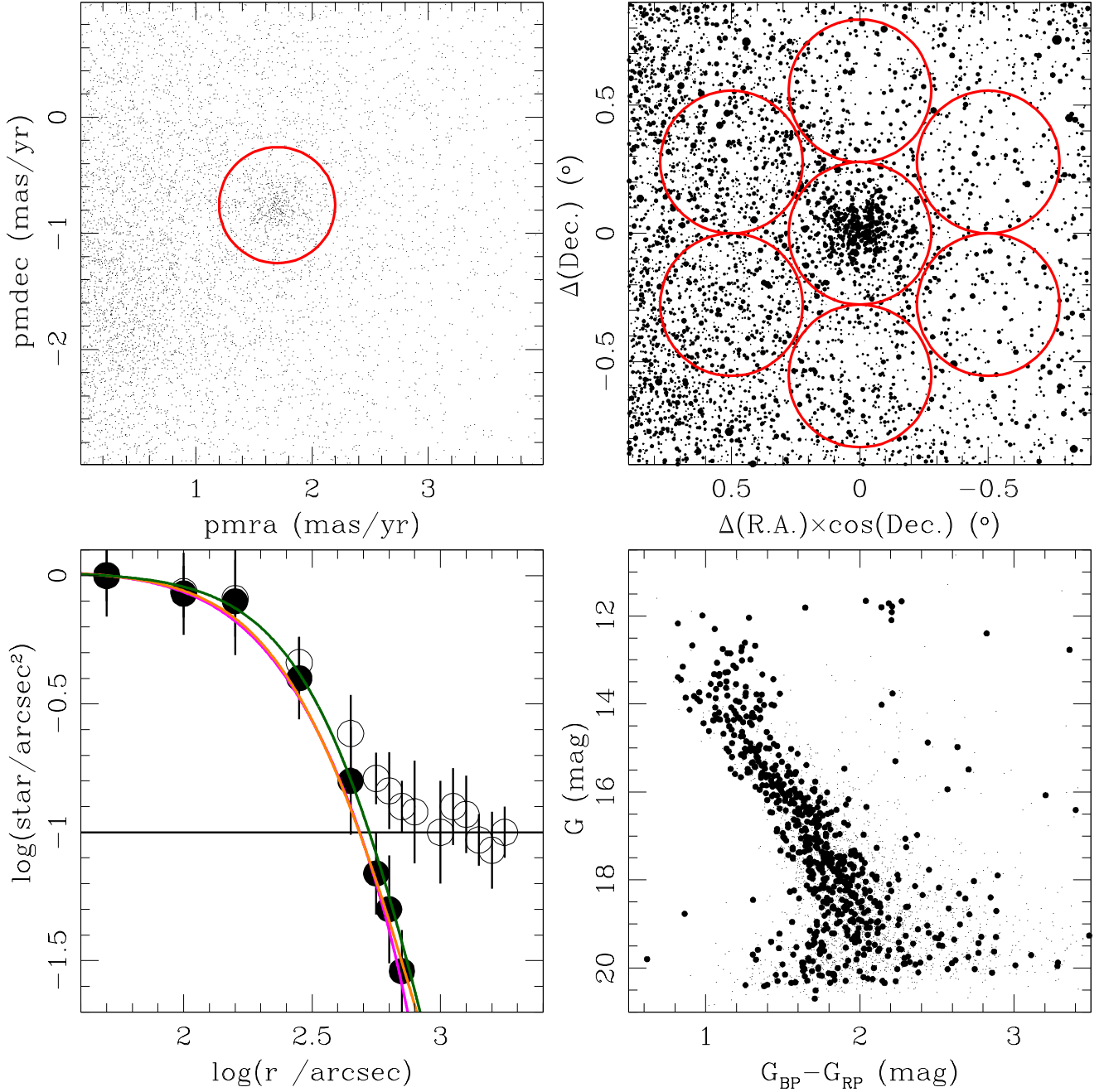


Figure 1. *Top-left panel:* Vector *Gaia* DR2's proper motions diagram of stars in the field of Collinder 347. The red circle's radius is 0.5 mas/yr. *Top-right panel:* Spatial distribution of stars located within the drawn circle in the vector proper motion diagram. The size of the symbols is proportional to the G mag. The red circles' radii are 0.28deg ($\log(r/\text{arcsec}) = 3$). *Bottom-left panel:* Normalised observed and background subtracted stellar density radial profiles drawn with open and filled symbols, respectively. The horizontal line corresponds to the adopted mean background level, while the magenta, orange and green lines are the best-fitted [King \(1962\)](#), [Plummer \(1911\)](#) and [Elson et al. \(1987\)](#) models, respectively. *Bottom-right:* cluster CMD for stars located within both, the circle in the vector proper motion diagram and the central cone in the finding chart drawn with large filled symbols; the small ones correspond to stars distributed within a radius of 0.84° from the cluster centre.

also hints at the existence of an eMSTO, as judged by the satisfactory match of the isochrone of $\log(t/\text{yr}) = 9.05$.

In order to quantify the extent of the eMSTO we counted the number of stars (N) located within the rectangle drawn in Fig. 4 (panel a), using as independent variable the

coordinate (X) along the long axis ([Goudfrooij et al. 2011](#); [Piatti 2013](#)). We then built the N distribution by summing all the individual X values. We represented each X value by a Gaussian function with centre and full-width half maximum equal to the X value and 2.355 times the associated

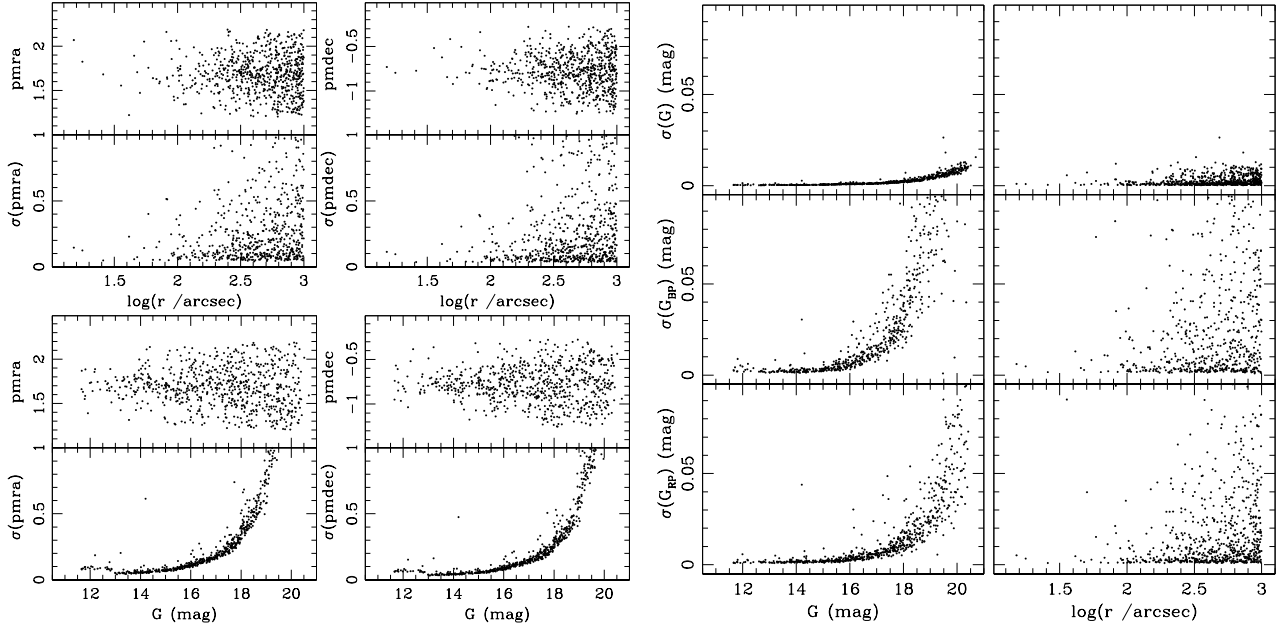


Figure 2. Kinematic and photometric data and their respective uncertainties as a function of the star brightness and distance from the cluster centre for stars located within both, the circle in the vector proper motion diagram and the central one in the finding chart (see Fig. 1).

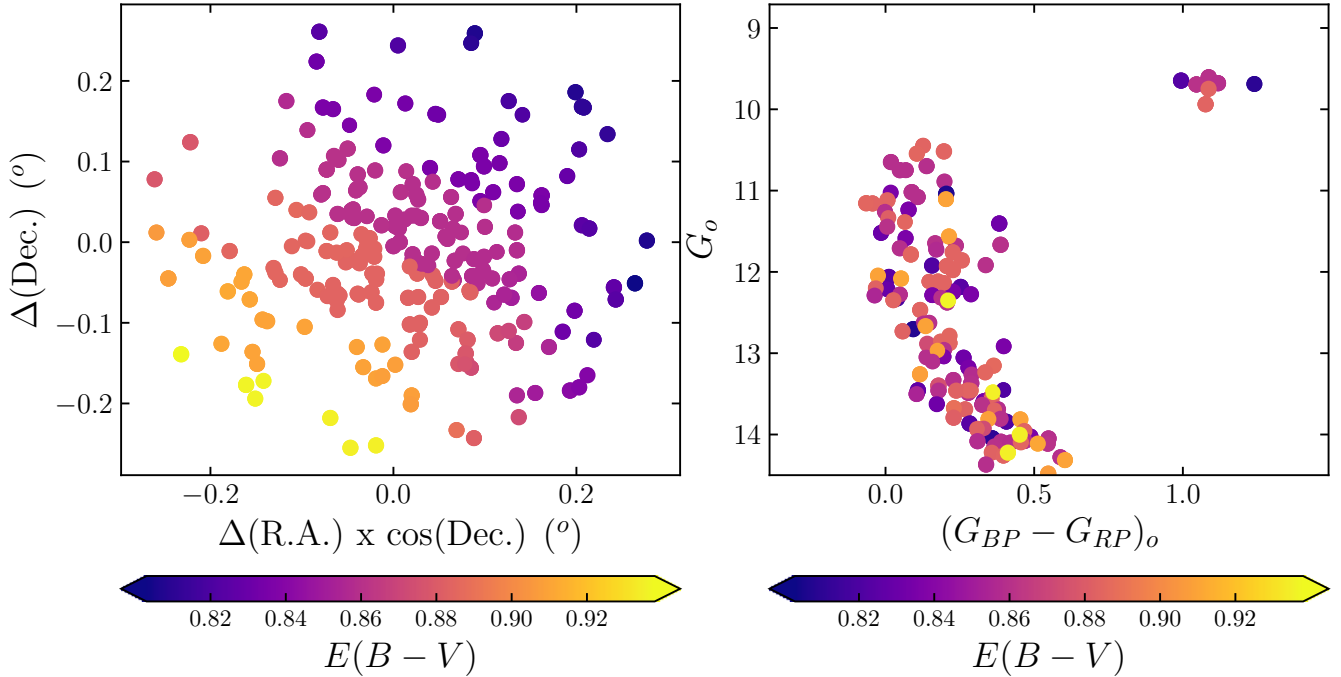


Figure 3. Spatial distribution (left panel) and cluster CMD (right panel) for stars with $P > 90$ per cent, on which our analysis relies. Colour-coded symbols represent the individual $E(B-V)$ values, while their sizes are proportional to $\sigma(E(B-V))$ in the range 0.095-0.0115 mag.

error $\sigma(X)$, respectively, and assigned to each Gaussian the same mean intensity. $\sigma(X)$ was computed taking into account the photometric errors (see Fig. 2) and the individual $E(B-V)$ errors. Thus, we avoid the problem of the histogram dependence on the bin size and the end points of

bin, which frequently lead to a difficulty in interpreting the results. The result is a continuous distribution – instead of a discrete histogram – that allows to appreciate the finest structures. Fig. 5 depicts the resulting N distribution with a black curve. As can be seen, a bimodal profile emerges,

with blue and red peaks at 600 ± 30 Myr and 1100 ± 30 Myr, respectively, as fitted by the IRAF.NGAUSSFIT routine. We then adopted as a mean eMSTO extent the difference between both mean values, i.e. 500 ± 60 Myr.

For completeness purposes, we exploited the *Gaia* DR2 data sets to build the cluster stellar radial density profile. We used all the stars retrieved in the $2^\circ \times 2^\circ$ region centred on the cluster with proper motions within the circle drawn in Fig. 1 (top-left panel) and brighter than $G = 18$ mag, to secure photometry completeness. We then counted the number of stars in rings centred on the cluster of width $15''$ up to $110''$ in steps of $15''$, and averaged all the constructed individual radial profiles. Fig. 1 (bottom-left panel) depicts the resulting radial profile with open circles, while the background subtracted one – the mean background level was estimated from rings far away the cluster region – is drawn with filled circles. We fitted King (1962), Plummer (1911) and Elson et al. (1987) models by χ^2 minimisation and obtained core (r_c), half-light (r_h) and tidal (r_t) radii of 1.60 ± 0.15 pc, 2.80 ± 0.15 pc and 8.00 ± 1.50 pc, respectively. The EFF’s power-law at large radii (γ) turned out to be 5.0 ± 0.5 .

If the cluster mass were confined to r_t , and a Milky Way mass enclosed at the cluster Galactocentric distance were assumed to be $\log(M(< R_{GC})) = 11.41 + 0.527 \times \log(R_{GC}) = 11.85$ (Taylor et al. 2016), the present-day cluster’s mass from Chernoff & Weinberg (1990) would result $(3.3\pm 1.8) \times 10^3 M_\odot$. From Lamers et al. (2005b, eqs. 2, 3, 7 and 11) and Lamers et al. (2005a, Table 1), we found that the fraction of initial mass still bound to the cluster is ~ 0.04 , after lived more than ~ 20 times its mean relaxation time $t_h = 32\pm 4$ Myr, computed from Spitzer & Hart (1971, eq. 5) for a mean MSTO stellar mass of $2.8 M_\odot$.

4 ANALYSIS AND DISCUSSION

The reddest MSTO stars observed in Fig. 4,a unlikely belong to the field, since every stars located within the cluster’s circle and with $P < 90$ per cent have intrinsic magnitudes and colours clearly different. Fig. 4,b depicts the loci of these stars with grey-coded symbols, where black and white filled circles corresponding to $85 < P$ (%) < 90 and $10 < P$ (%) < 15 , respectively. We thoroughly also investigated whether the photometric errors and the individual stellar reddening errors could blur such an eMSTO. To assess on this effect we performed Monte Carlo simulations to generate a thousand CMDs per star with $P > 90$ per cent, allowing that star to have random intrinsic magnitudes and colours within the interval $[-\Delta(G), +\Delta(G)]$ and $[-\Delta(G_{BP} - G_{RP}), +\Delta(G_{BP} - G_{RP})]$, respectively. We computed:

$$\Delta(G) = [\sigma_G^2 + (2.44 \sigma_{E(B-V)})^2]^{1/2},$$

$$\Delta(G_{BP} - G_{RP}) = [\sigma_{G_{BP}}^2 + \sigma_{G_{RP}}^2 + (1.27 \sigma_{E(B-V)})^2]^{1/2},$$

where σ represents the errors in each quantity. From a total of 227000 generated CMDs we built the Hess diagram of Fig. 6, which still exhibits the eMSTO seen in Fig. 4. Note that with more accurate reddening estimates, the eMSTO feature would have resulted even more visible.

The combined effect of stellar binarity and photometric

errors was evaluated through the generation of a synthetic CMD for a cluster with a total mass of $5 \times 10^3 M_\odot$ and age and metal content as for Collinder 347. We used SYCLIST² (Ekström et al. 2012; Georgy et al. 2014) and PADOVA.CMD³ (Bressan et al. 2012) packages and assumed a binary fraction of 0.5 (Milone et al. 2016; Piatti & Cole 2017). The resulting synthetic CMD is shown in Fig. 4,c where we superimposed two theoretical isochrones (Bressan et al. 2012) embracing the observed spread. Following the same procedure described above to estimate the observed MSTO extent, we obtained from the synthetic CMD $\Delta(\text{age}) = 230\pm 30$ Myr.

We also dealt with metallicity spread using a subset of isochrones, which assume $Y = 0.2485 + 1.78Z$ (see Fig. 4,d). Note that we assumed an arbitrary amount of metallicity and helium content variations, aiming at illustrating for completeness purposes that they do not impact on the MSTO extent. Indeed, as far as we are aware, there is no evidence of metallicity and helium spread in Milky Way open clusters (Donor et al. 2018). In this case, we adopted $\Delta(\text{age}) = 50\pm 10$ Myr.

As for estimating the magnitude of stellar rotation effects, we made use of the relationship obtained by Niederhofer et al. (2015) between the age of a star cluster and the expected (apparent) age spread. Thus, by interpolating an age of $\log(t/\text{yr}) = 8.8$ in their Fig. 2, we obtained $\Delta(\text{age}) = 250\pm 40$ Myr. High fraction of Be stars that implies a high fraction of rapidly rotating stars have been found in Milky Way open clusters and Magellanic Cloud clusters (Bastian et al. 2017; Milone et al. 2018). As H α contributes to the three *Gaia* DR2 bandpasses⁴, and hence it is in principle cancelled through the $G_{BP} - G_{RP}$ colour, the observed broadness – particularly the reddest stars around $G_o \approx 12.0$ mag and $(G_{BP} - G_{RP})_o \sim 0.25$ mag – confirms that the observed spread is not mainly caused by rapid rotators.

Finally, we added in quadrature all the apparent age spreads by approximating them to Gaussian distributions (see Piatti & Cole 2017), namely, that from observational errors and stellar binarity (230 Myr), that from stellar rotation (250 Myr), and that from iron-helium variations (50 Myr), to obtain an overall apparent age spread of 340 ± 50 Myr. As can be seen, the resulting value is clearly smaller than the observed one of 500 ± 60 Myr. The difference between the mean values is 160 Myr, clearly smaller than the sum of their respective uncertainties (100 Myr). Moreover, if we subtracted them in quadrature, then the intrinsic age spread would turn out to be 360 ± 130 Myr. This extended observed age spread points to the need of considering stellar populations with different ages could populate Collinder 347.

ACKNOWLEDGEMENTS

We thank Mateus Angelo and Wilton Dias because their work inspired us to dig into the *Gaia*’ archive, and Dafydd Evans to provided me with feedback about *Gaia*’s photometry completeness. This work presents results from the European Space Agency (ESA) space mission *Gaia*. *Gaia* data

² <https://www.unige.ch/sciences/astro/evolution/en/database/syclist/>

³ <http://stev.oapd.inaf.it/cgi-bin/cmd>

⁴ https://www.cosmos.esa.int/web/gaia/iow_20180316

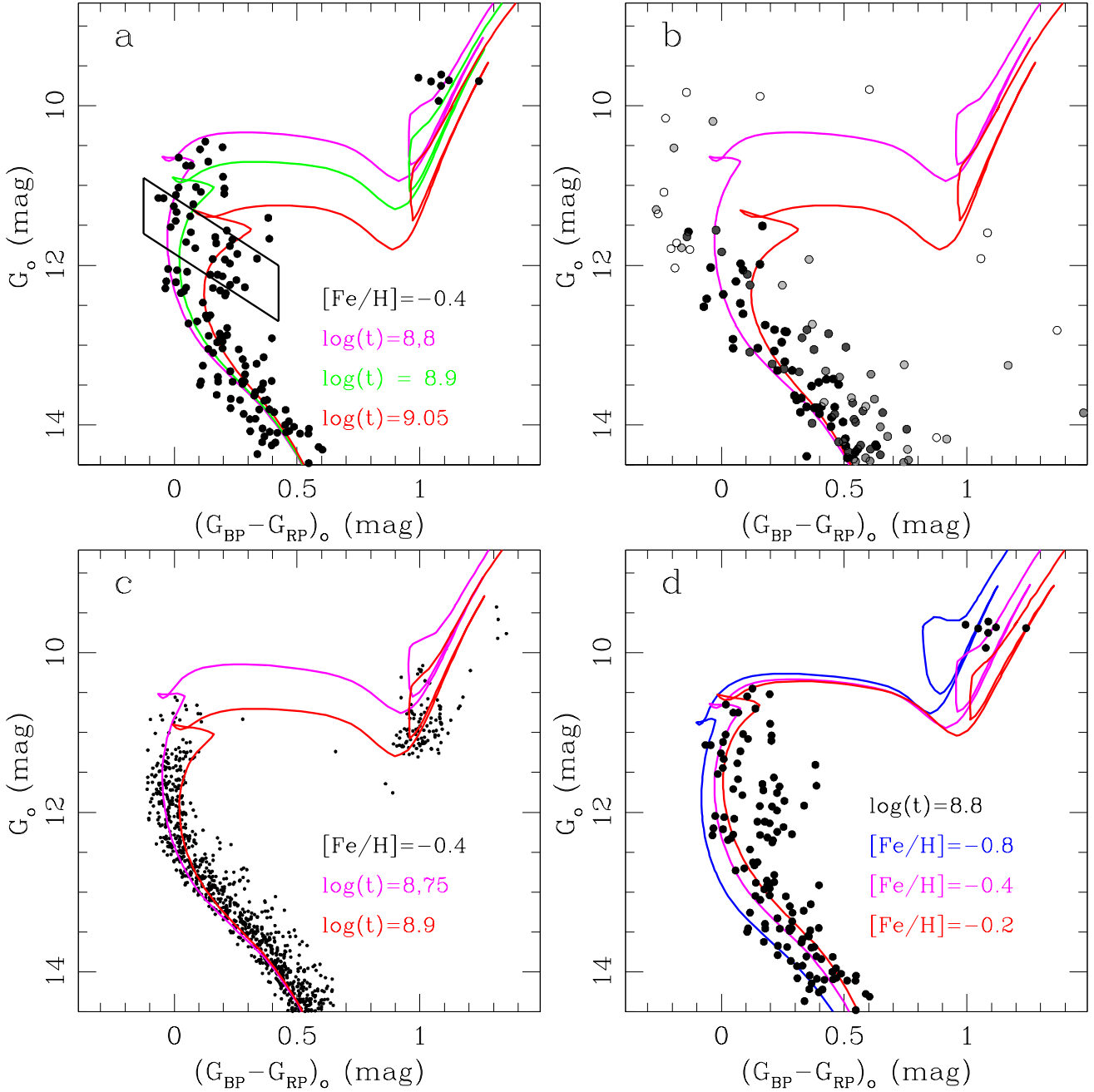


Figure 4. Cleaned intrinsic cluster CMD for stars with $P > 90$ per cent (panel a) and stars with $P < 90$ per cent (panel b). A rectangle scanning the eMSTO region is also superimposed (panel a). Both panels show the same isochrones superimposed. A synthetic CMD is shown in panel c, while panel d is the same as panel a with different set of isochrones overlotted (see text for details).

are being processed by the Gaia Data Processing and Analysis Consortium (DPAC). Funding for the DPAC is provided by national institutions, in particular the institutions participating in the Gaia MultiLateral Agreement (MLA). The Gaia mission website is <https://www.cosmos.esa.int/gaia>. The Gaia archive website is <https://archives.esac.esa.int/gaia>.

REFERENCES

- Arenou F., et al., 2018, *A&A*, **616**, A17
 Bastian N., et al., 2017, *MNRAS*, **465**, 4795
 Bastian N., Kamann S., Cabrera-Ziri I., Georgy C., Ekström S., Charbonnel C., de Juan Ovelar M., Usher C., 2018, *MNRAS*, **480**, 3739
 Bressan A., Marigo P., Girardi L., Salasnich B., Dal Cero C., Rubele S., Nanni A., 2012, *MNRAS*, **427**, 127
 Bukowiecki L., Maciejewski G., Konorski P., Strobel A., 2011, *Acta Astron.*, **61**, 231

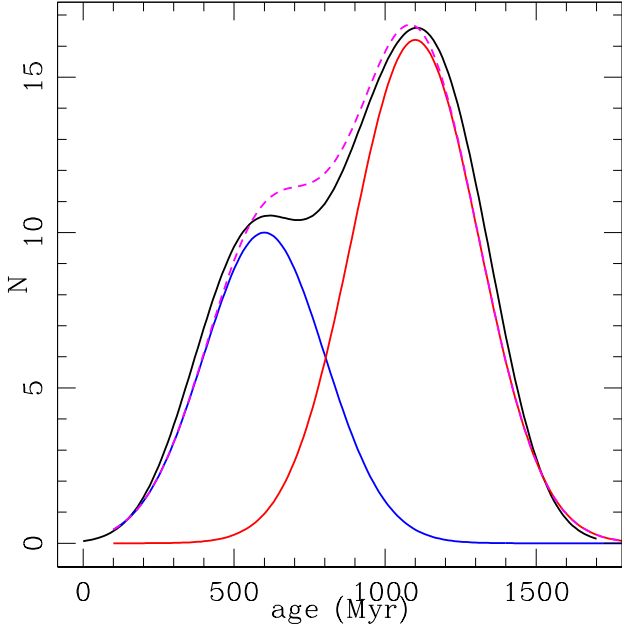


Figure 5. Number of stars counted along the major axis of the rectangle drawn in Fig. 4 shown with a black curve. Blue and red curves represent the fitted Gaussians to the observed bimodal distribution, while the dashed magenta curve is the sum of both of them.

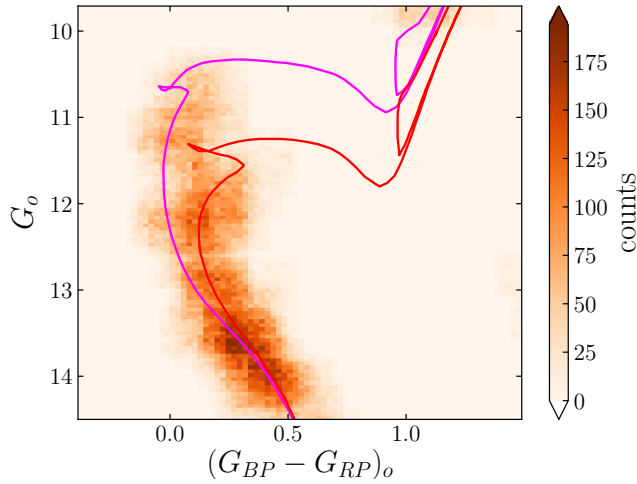


Figure 6. Hess diagram of Fig. 4 (panel a) generated considering photometric errors and individual stellar $E(B - V)$ errors.

Ekström S., et al., 2012, *A&A*, 537, A146
 Elson R. A. W., Fall S. M., Freeman K. C., 1987, *ApJ*, 323, 54
 Georgy C., Granada A., Ekström S., Meynet G., Anderson R. I., Wyttenbach A., Eggenberger P., Maeder A., 2014, *A&A*, 566, A21
 Georgy C., et al., 2019, *A&A*, 622, A66
 Gossage S., et al., 2019, arXiv e-prints, p. arXiv:1907.11251
 Goudfrooij P., Puzia T. H., Kozhurina-Platais V., Chandar R., 2011, *ApJ*, 737, 3
 Goudfrooij P., Girardi L., Bellini A., Bressan A., Correnti M., Costa G., 2018, *ApJ*, 864, L3
 Heiter U., Soubiran C., Netopil M., Paunzen E., 2014, *A&A*, 561, A93
 Kharchenko N. V., Piskunov A. E., Schilbach E., Röser S., Scholz R. D., 2013, *A&A*, 558, A53
 King I., 1962, *AJ*, 67, 471
 Lallement R., Babusiaux C., Vergely J. L., Katz D., Arenou F., Valette B., Hottier C., Capitanio L., 2019, *A&A*, 625, A135
 Lamers H. J. G. L. M., Gieles M., Portegies Zwart S. F., 2005a, *A&A*, 429, 173
 Lamers H. J. G. L. M., Gieles M., Bastian N., Baumgardt H., Kharchenko N. V., Portegies Zwart S., 2005b, *A&A*, 441, 117
 Li C., Sun W., de Grijs R., Deng L., Wang K., Cordoni G., Milone A. P., 2019, *ApJ*, 876, 65
 Lindegren L., et al., 2018, *A&A*, 616, A2
 Marino A. F., Przybilla N., Milone A. P., Da Costa G., D’Antona F., Dotter A., Dupree A., 2018a, *AJ*, 156, 116
 Marino A. F., Milone A. P., Casagrande L., Przybilla N., Balaguer-Núñez L., Di Criscienzo M., Serenelli A., Vilardeff F., 2018b, *ApJ*, 863, L33
 Milone A. P., Marino A. F., D’Antona F., Bedin L. R., Da Costa G. S., Jerjen H., Mackey A. D., 2016, *MNRAS*, 458, 4368
 Milone A. P., et al., 2018, *MNRAS*, 477, 2640
 Niederhofer F., Georgy C., Bastian N., Ekström S., 2015, *MNRAS*, 453, 2070
 Piatti A. E., 2013, *MNRAS*, 430, 2358
 Piatti A. E., Bica E., 2012, *MNRAS*, 425, 3085
 Piatti A. E., Cole A., 2017, *MNRAS*, 470, L77
 Piatti A. E., Cole A. A., Emptage B., 2018, *MNRAS*, 473, 105
 Piatti A. E., Alfaro E. J., Cantat-Gaudin T., 2019, *MNRAS*, 484, L19
 Plummer H. C., 1911, *MNRAS*, 71, 460
 Spitzer Jr. L., Hart M. H., 1971, *ApJ*, 164, 399
 Sun W., de Grijs R., Deng L., Albrow M. D., 2019, *ApJ*, 876, 113
 Taylor C., Boylan-Kolchin M., Torrey P., Vogelsberger M., Hernquist L., 2016, *MNRAS*, 461, 3483
 Wang S., Chen X., 2019, *ApJ*, 877, 116

This paper has been typeset from a $\text{\TeX}/\text{\LaTeX}$ file prepared by the author.

Cardelli J. A., Clayton G. C., Mathis J. S., 1989, *ApJ*, 345, 245
 Chernoff D. F., Weinberg M. D., 1990, *ApJ*, 351, 121
 Clariá J. J., Parisi M. C., Palma T., Ahumada A. V., Oviedo C. G., 2019, *Acta Astron.*, 69, 1
 Cordoni G., Milone A. P., Marino A. F., Di Criscienzo M., D’Antona F., Dotter A., Lagioia E. P., Tailo M., 2018, *ApJ*, 869, 139
 D’Antona F., Milone A. P., Tailo M., Ventura P., Vesperini E., di Criscienzo M., 2017, *Nature Astronomy*, 1, 0186
 Donor J., et al., 2018, *The Astronomical Journal*, 156, 142
 Dupree A. K., et al., 2017, *ApJ*, 846, L1